

# Ultra-Precise High-Speed Untethered Manipulation of Magnetic Scanning Microprobe in Aqueous Solutions

Ta-Min Meng  and Chia-Hsiang Menq 

**Abstract**— This article describes the design and development of an integrated system that renders ultra-precise and high-speed, untethered manipulation of a single magnetic scanning microprobe in aqueous solutions under a microscope. The system uses a six-input-three-output hexapole electromagnetic actuator to control the magnetic gradient force exerted on the probe and a three-dimensional vision-based motion tracking system to enable feedback control. The control system has three core functions that enables superior manipulation of the magnetic microprobe. The six-input-six-output closed-loop magnetic flux control significantly suppresses the effect of magnetic hysteresis and greatly increases the bandwidth of magnetic flux generation. The optimal flux allocation solves four issues in multipole magnetic force generation: redundancy; coupling; nonlinearity; and position-dependency. The position-dependent discrete-time motion control law determines the required force for stabilization and tracking. These three core functions have been implemented using a high-speed field programmable gate array (FPGA) system. Experiments have verified that the use of digital control technology, high-speed electronics, mathematical modeling, and real-time computation has achieved superior manipulation of a single magnetic microprobe in aqueous solutions.

**Index Terms**— Electromagnetic actuation, magnetic flux control, motion tracking, untethered manipulation.

## I. INTRODUCTION

APPLYING scanning probe microscopy (SPM) to scan biological samples and to manipulate biological processes has become an important technique for the studies of cell mechanics and mechanobiology [1]. Atomic force microscopy (AFM) provides high spatial resolution and is capable of force sensing, but there are major limitations when applied to probe

Manuscript received 26 February 2022; revised 22 June 2022; accepted 30 July 2022. Date of publication 18 August 2022; date of current version 16 February 2023. Recommended by Technical Editor C. E. Okwudire and Senior Editor X. Tan. This work was supported in part by the endowment fund for the Ralph W. Kurtz Chair in Mechanical Engineering at the Ohio State University. (*Corresponding author:* Chia-Hsiang Menq.)

The authors are with the Department of Mechanical and Aerospace Engineering, The Ohio State University, Columbus, OH 43210 USA (email: meng.350@osu.edu; menq.1@osu.edu).

Color versions of one or more figures in this article are available at <https://doi.org/10.1109/TMECH.2022.3196596>.

Digital Object Identifier 10.1109/TMECH.2022.3196596

biological samples. It is a two-dimensional (2-D) surface tool, mainly applied to obtain surface topography and micromechanical property of planar surfaces [2]. The typical scan range ( $\sim 10 \mu\text{m}$ ) and speed (one line per second) are inadequate for live cell ( $\sim 30 \mu\text{m}$ ) applications. Due to the restriction of mechanical connections, it is not suitable for intracellular applications. When operating in aqueous solution, the force resolution of a typical AFM probing system is at best several-tens of piconewtons ( $p\text{N}$ ).

Optical trapping is another useful modern technique for the studies of biological systems under physiological conditions [3]–[5], but there are key barriers inhibiting its applications to the study of live biological systems. The typical spatial range ( $\sim 1 \mu\text{m}$ ) is very limited. Although increasing laser power to trap small objects has been demonstrated, heating is a main issue that needs to be resolved [6]–[8]. Furthermore, the specificity of optical trapping in controlling the probe is in doubt. Unwanted trap of debris may easily mix with the probe. Despite these issues, optical tweezers have gained their popularity due to one distinct advantage, i.e., a stable trap is readily established for a microscopic dielectric object [9], [10].

Multipole electromagnetic actuators are widely used in a variety of applications, including magnetic levitation of multiaxis motion devices [11], [12], propulsion of miniature swimming machines [13], [14], and multiaxis scanning probe technology [15], [16]. They have recently been implemented as magnetic tweezers to enable untethered manipulation of microprobes [17] and employed to probe biological processes with interaction forces ranging from sub-piconewtons to tens of piconewtons scales [18]. Most existing magnetic tweezers are simple force applicators/transducers. In a typical experiment, one attaches magnetic particles to molecules of interest and then applies an external magnetic field to exert a force ( $\sim p\text{N}$ ) for quasi-static measurement of tensile strength of or binding forces between molecules [19]–[21]. Although these setups are popular bio-physical tools, their application is limited to simple experiments on isolated biological samples.

Recently, hexapole electromagnetic actuators have been developed, in which six pointed poles, each driven by a separate coil, are employed to enable the generation of 3-D forces [22], [23]. They are six-input-three-output nonlinear actuators. The optimal current allocation [24] associated with hexapole actuation has been devised to achieve the inverse modeling

required for magnetic force generation. It was implemented to realize real-time current allocation, thereby enabling current-based control of the probing system. Together with vision-based particle tracking systems, a visual servo control system has been developed to enable 3-D magnetic actuation and stable trapping of individual magnetic microprobes in aqueous solutions [24], illustrating the potential of providing scanning probe functionality using magnetic tweezer technology.

The hexapole actuator uses the six input currents to produce magnetic fluxes at the six pole tips to control the magnetic field in the 3-D workspace and the 3-D magnetic gradient force exerted on the magnetic probe. The current-based model uses a quasi-static relationship between the actuation current and the generated magnetic flux, which ignores the history-dependent nonlinearity, i.e., hysteresis, in and the eddy-current-induced dynamics in magnetic flux generation. While the current-based control enables stable magnetic trapping and visual-servo control [22]–[24], hysteresis and dynamics of flux generation cannot be ignored when the scanning probe function requires high-speed and precise steering of the magnetic microprobe.

This article describes the design and development of an integrated system that renders ultra-precise and high-speed untethered manipulation of a single magnetic scanning probe in aqueous solutions under a microscope. The integrated system uses previously developed hexapole actuator [23] and an improved motion tracking system to form a high-speed 3-D visual servo control system. Three core functions of the system are designed and implemented for precise steering of the magnetic microprobe at high-speeds to enable 3-D scanning. They are the closed-loop magnetic flux control, the optimal voltage allocation, and the discrete-time motion control law. Three major contributions are identified and briefly summarized below.

First, the dynamics for the hexapole magnetic flux generation were characterized with a second order six-input-six-output model through experimentation with a previous Hall-sensor integrated actuator [25]. Based on the dynamic model, a six-input-six-output magnetic flux control system was developed to solve the three issues in current-based flux generation [22], [24]: multipole coupling; uncertainty due to magnetic hysteresis; and limited bandwidth. With six-input-six-output flux control, the magnetic flux at each individual pole tip can be precisely controlled at frequencies up to 1000 Hz (see Section II-C). Second, the flux allocation proposed in [25] has been integrated with six-input-six-output magnetic flux control such that the six-input hexapole system behaves like a decoupled three-axis force producer with a bandwidth of 1000 Hz (see Section II-D). Third, in contrast to using proportional (P) control for positioning [22]–[25] and proportional and integral (PI) control for slow-motion tracking [22]–[25], a model-based position-dependent control law was derived and implemented to achieve high-speed manipulation of the magnetic microprobe in aqueous solutions, where the motion error is zero-mean random error, which is dictated by both random thermal forces and random

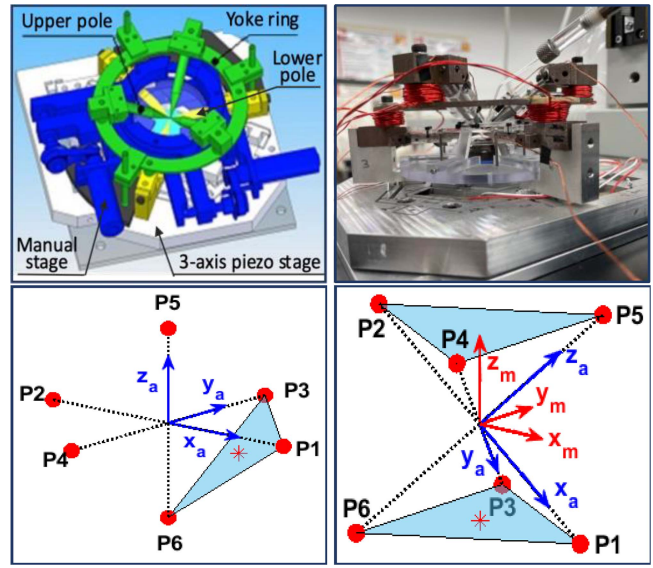


**Fig. 1.** Upper left panel shows the CAD model of the hexapole system. The upper right panel shows a prototype of the hexapole electromagnetic actuator. The bottom left panel illustrates the symmetric arrangement of the six pole tips. The bottom right panel shows the relationship between the actuation coordinate system and the measurement coordinate system.

measurement noise (see Section III). Experimental verification of ultra-precise and high-speed manipulation is presented in Section IV.

## II. CONTROL OF THREE-DIMENSIONAL MAGNETIC FORCE

This section discusses the generation and control of 3-D magnetic gradient forces using a hexapole electromagnetic actuation system. The generation of 3-D magnetic force is probe-specific and requires precise control to achieve superior untethered manipulation of the magnetic microprobe.

### A. Generation of 3-D Magnetic Force

The two upper panels of Fig. 1 show the design and prototype of a hexapole electromagnetic actuation system [23]. Three pairs of pointed electromagnetic poles are assembled to concentrate the magnetic flux into the workspace, where the sample and the moving magnetic probe are placed. Two coordinate systems, i.e., the measurement coordinate system and the actuation coordinate system, are defined for measurement and actuation modeling, respectively. The  $z$ -axis for the measurement coordinate system is aligned with the optical axis of the microscope (Olympus IX 81) employed for the particle tracking. The tips of the six poles are placed symmetrically on three orthogonal axes initially aligned with the measurement coordinate system, shown in the bottom left panel, to enclose the 3-D workspace. Specifically,  $P_2 \rightarrow P_1$ ,  $P_4 \rightarrow P_3$  and  $P_6 \rightarrow P_5$  delineate the three axes of the actuation coordinate system, i.e.,  $+x$ ,  $+y$ , and  $+z$ . By rotating the six poles about the  $x$ -axis by  $-45^\circ$  and then about the  $y$ -axis by  $35^\circ$ , the tips of the six poles are on two parallel horizontal planes in the measurement coordinate system, i.e., one upper

plane and the other lower plane, shown in the bottom right panel, and the blockage of the optical path is avoided.

Each pole is driven by a separate coil. All coils and poles are magnetically connected by yokes. Once the controlled current is applied to its coil, the magnetic flux  $\Phi$  permeates through all poles to pole tips. The workspace is a polyhedron, whose size is determined by the distance between each individual pole tip and the center, denoted by  $\ell$ . Although  $\ell$  is adjustable, for all experiments reported in Sections III and IV, it is 500 micrometers. The probes used in all experiments are ferromagnetic spheres with a diameter of 4.5 micrometers. The hexapole system is used to generate and exert 3-D forces on the magnetic probe. A quadratic form relating the magnetic flux at the tips of the six poles to the 3-D magnetic gradient force has been derived and used as a kernel for modeling force generation [25]. It is expressed with respect to the actuator coordinate system

$${}^A\mathbf{f}_m({}^A\mathbf{p}, \boldsymbol{\phi}) = g_\phi \boldsymbol{\phi}^T \mathbf{L}(\hat{\mathbf{p}}) \boldsymbol{\phi} = g_\phi \begin{bmatrix} \boldsymbol{\phi}^T \mathbf{L}_x(\hat{\mathbf{p}}) \boldsymbol{\phi} \\ \boldsymbol{\phi}^T \mathbf{L}_y(\hat{\mathbf{p}}) \boldsymbol{\phi} \\ \boldsymbol{\phi}^T \mathbf{L}_z(\hat{\mathbf{p}}) \boldsymbol{\phi} \end{bmatrix}, \quad (1)$$

where  ${}^A\mathbf{f}_m$  is the 3-D magnetic force,  ${}^A\mathbf{p}$  is the position of the probe,  $\boldsymbol{\phi} = [\phi_1 \phi_2 \phi_3 \phi_4 \phi_5 \phi_6]^T$  is the  $6 \times 1$  magnetic-flux vector, and  $g_\phi$  denotes the force gain associated with the flux vector. The gradient matrix,  $\mathbf{L}$  [23], [24], consists of three  $6 \times 6$  matrices,  $\mathbf{L}_x$ ,  $\mathbf{L}_y$ , and  $\mathbf{L}_z$ . Each entry of the  $6 \times 6 \times 3$  gradient matrix is a function of the dimensionless position,  $\hat{\mathbf{p}} = {}^A\mathbf{p}/\ell$ , normalized with respect to the radius of the workspace. The gradient matrix depicts the redundancy, multipole coupling, position-dependance of the six-input-three-output force generation system. It is worth noting that  $g_\phi$  is inversely proportional to the fifth power of  $\ell$ , and is probe-specific, i.e., proportional to the volume and susceptibility of the probe.

The magnetic flux is produced by the magnetomotive force, which is proportional to the input current  $\mathbf{I}$ , and the turns of the coil,  $N_c$ . By Hopkinson's law in magnetic circuit analysis, the magnetic flux is quasi-statically related to the input current by  $\boldsymbol{\phi}_I = (N_c/\mathcal{R}_a) \mathbf{K}_I \mathbf{I}$ , where  $\mathcal{R}_a$  is the lumped magnetic reluctance and  $\mathbf{K}_I$  is the  $6 \times 6$  flux distribution matrix. This approach has led to current-based magnetic force models [22], [23], which can be derived from (1)

$${}^M\mathbf{f}_m({}^M\mathbf{p}, \mathbf{I}) = g_I {}^M\mathbf{R} [\mathbf{I}^T \mathbf{K}_I^T \mathbf{L}({}^M\mathbf{R} {}^M\mathbf{p}/\ell) \mathbf{K}_I \mathbf{I}], \quad (2)$$

where  $g_I = (N_c/\mathcal{R}_a)^2 g_\phi$  is the force gain associated with the current vector. The current-based force model has two major limitations: suffering from uncertainty attributed to hysteresis in magnetic flux generation and ignoring the dynamic of magnetic flux generation.

The flux vector  $\boldsymbol{\phi}$  associated with the hexapole actuator is not readily available. It can, however, be measured using Hall sensors. By placing six Hall sensors (Asahi Kasei EQ-730L) in total, one on the surface of each pole, to measure the magnetic flux at the tip of each pole, the flux vector is related to the readings of the six Hall sensors by  $\boldsymbol{\phi} = \mathbf{D}_H \mathbf{v}_H$ , where  $\mathbf{D}_H$  is a diagonal voltage-flux gain matrix and  $\mathbf{v}_H$  is the sensor-voltage vector [25]. Normalizing  $\mathbf{D}_H$ ,  $\hat{\mathbf{D}}_H = \mathbf{D}_H/\|\mathbf{D}_H\|$ , the

Hall-sensor-based hexapole magnetic force model can be derived from (1)

$${}^M\mathbf{f}_m({}^M\mathbf{p}, \mathbf{v}_H) = g_H {}^M\mathbf{R} \left[ \mathbf{v}_H^T \hat{\mathbf{D}}_H^T \mathbf{L}({}^M\mathbf{R} {}^M\mathbf{p}/\ell) \hat{\mathbf{D}}_H \mathbf{v}_H \right], \quad (3)$$

where  $g_H = \|\mathbf{D}_H\|^2 g_\phi$  is the force gain associated with the sensor-voltage vector.

### B. Optimal Flux Allocation

The hexapole actuation system is an over-actuated (six input three output) and strongly coupled nonlinear system. Assigning the  $6 \times 1$  controllable variables  $\mathbf{v}_d$  that generate the  $3 \times 1$  desired actuation force is a challenging task, but also essential for the practical use of the actuation system. In addition, the generation of magnetic force is position-dependent and the allocation of  $\mathbf{v}_d$  needs to be done in real time. The optimal flux allocation reported in [25] employs analytical derivation, constrained optimization, numerical calculation, and least square fitting to obtain the optimal flux allocation, minimizing the two-norm of the magnetic flux vector,  $\boldsymbol{\phi}^T \boldsymbol{\phi}$ , to render accurate and effective 3-D force generation for real-time applications. Since the nonlinear relationship between the magnetic force and the magnetic flux is a quadratic form, using the spherical coordinates of the desired force,  ${}^A\mathbf{f}_d = f_d \hat{\mathbf{r}}(\varphi, \theta)$ , where  $f_d$  is the magnitude and  $\hat{\mathbf{r}}(\varphi, \theta)$  is the unit radial vector, leads to a scalable optimal solution,  $\hat{\boldsymbol{\phi}}_{opt}(\varphi, \theta, {}^A\hat{\mathbf{p}})$ , yielding the desired unit force,  $\hat{\mathbf{r}}(\varphi, \theta)$ . This scalable relationship renders the focus on the direction of the desired force when finding the optimal flux allocation. It is essentially an optimization problem under nonlinear equality constraints.

MATLAB optimization toolbox was used to numerically determine the optimal solutions at predetermined positions covering the desired spatial range in the 3-D workspace and along specific discrete directions  $\hat{\mathbf{r}}(\varphi_j, \theta_j)$ . Least squares fitting was then employed to construct an analytical direction-dependent  $6 \times 4 \times 4$  optimal flux-allocation matrix,  $\mathbf{D}^{LS}(\varphi, \theta)$  [25] to serve as a kernel for optimal magnetic flux allocation

$$\hat{\boldsymbol{\phi}}_{opt}(\varphi, \theta, {}^A\hat{\mathbf{p}}) \approx \hat{\mathbf{P}}^T \mathbf{D}^{LS}(\varphi, \theta) \hat{\mathbf{P}}, \quad (4)$$

where  $\hat{\mathbf{P}} = [\hat{x}, \hat{y}, \hat{z}, 1]^T$  is the augmented position vector. With  $\hat{\boldsymbol{\phi}}_{opt}(\varphi, \theta, {}^A\hat{\mathbf{p}})$ , one can then calculate optimal flux allocation, i.e.,  $\boldsymbol{\phi}_{opt}({}^A\mathbf{f}_d, {}^A\hat{\mathbf{p}}) = \sqrt{f_d/g_\phi} \hat{\boldsymbol{\phi}}_{opt}(\varphi, \theta, {}^A\hat{\mathbf{p}})$ , via scaling to produce  ${}^A\mathbf{f}_d$ . It can then be used to calculate optimal current allocation or optimal voltage allocation for force generation

$$\begin{aligned} \mathbf{I}_{opt}({}^A\mathbf{f}_d, {}^A\hat{\mathbf{p}}) &= \sqrt{\frac{f_d}{g_I}} \mathbf{K}_I^{-1} \hat{\boldsymbol{\phi}}_{opt}(\varphi, \theta, {}^A\hat{\mathbf{p}}) \\ \mathbf{v}_{opt}({}^A\mathbf{f}_d, {}^A\hat{\mathbf{p}}) &= \sqrt{\frac{f_d}{g_H}} \hat{\mathbf{D}}_H^{-1} \hat{\boldsymbol{\phi}}_{opt}(\varphi, \theta, {}^A\hat{\mathbf{p}}) \end{aligned} . \quad (5)$$

### C. Six-Input-Six-Output Magnetic Flux Control System

To overcome the limitations of current-based magnetic flux generation, the six Hall sensors are connected to a high-speed field programmable gate array (FPGA) system through AD converters to enable magnetic flux control, aiming to achieve precise generation and control of the magnetic force exerted on

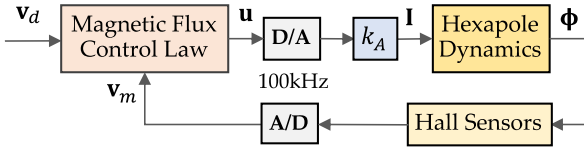


Fig. 2. Block diagram of the six-input-six-output magnetic flux control system.

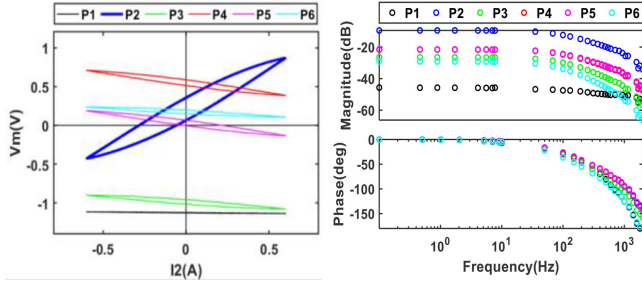


Fig. 3. Experimental results of open-loop flux generation experiment.

the magnetic probe. Fig. 2 shows the block diagram of the six-input-six-output magnetic flux control system, where  $k_A$  is the gain of the linear amplifiers (Micro Dynamics, BTA-28V-6A), whose bandwidth is 10 kHz. Based on the allocated voltage  $v_d$  and Hall-sensor measurement  $v_m$ , the flux control law actively adjusts the six actuation currents to control the magnetic flux at the six pole tips.

Fig. 3 presents the experimental results of open-loop magnetic flux generation. The left panel presents the voltage readings of the six Hall sensors vs. a single 0.1 Hz input current applied to pole 2 (P2). It clearly shows multipole coupling, bias, and hysteresis in magnetic flux generation. In the experiment, the frequency was increased from 0.1 to 1.6 kHz. The voltage readings were recorded. The discrete frequency spectrum was calculated using FFT to verify that the dominant frequency is the excitation frequency and to remove the bias. The dominant frequency components were then used to calculate amplitude ratios and phase lags to form six frequency response curves, presented in the right panel of Fig. 3. It shows that when focusing on the dominant frequency components of the dynamic response, despite the presence of multipole coupling, the dynamic characteristics of magnetic flux generation can be clearly seen, e.g., a bandwidth of about 160 Hz.

Six single-pole excitations were tested, each producing six sets of amplitude ratios and phase lags. All 36 sets were then used to fit a second order six-input-six-output discrete model

$$\mathbf{v}_m[k+1] = a_1 \mathbf{v}_m[k] + a_2 \mathbf{v}_m[k-1] + \mathbf{B}[\mathbf{u}[k] + \mathbf{w}[k]], \quad (6)$$

where  $\mathbf{v}_m$  is the  $6 \times 1$  sensor-voltage vector (denoted as  $\mathbf{v}_H$  in (3)),  $\mathbf{u}$  the  $6 \times 1$  vector consisting of the six input voltages being sent to the D/A converter to produce six actuation currents, and  $\mathbf{B}$  the  $6 \times 6$  input matrix. The discrete system model has two poles,  $p_1 = 0.9898$  and  $p_2 = 0.6053$ . Since the discrete dominate pole in the z-plane is  $p_1 = 0.9898$  and as the sampling rate is 100 kHz, the bandwidth of the magnetic flux generation is

estimated to be 163 Hz. The combined effects of modeling error and remanence appear as disturbances,  $\mathbf{w}$ .

The control objective is  $\delta \mathbf{v}[k+1] = \lambda_c \delta \mathbf{v}[k]$ , where  $0 \leq \lambda_c < 1$  and  $\delta \mathbf{v}$  is the tracking error,  $\delta \mathbf{v}[k] = \mathbf{v}_d[k] - \mathbf{v}_m[k]$ . Using one-step preview to realize feedforward control,  $\mathbf{v}_{ff}[k] = \mathbf{v}_d[k+1] - a_1 \mathbf{v}_d[k] - a_2 \mathbf{v}_d[k-1]$ , employing the estimated tracking error  $\hat{\delta} \mathbf{v}$  for feedback control,  $\delta \mathbf{v}_{fb}[k] = (a_1 - \lambda_c) \hat{\delta} \mathbf{v}[k] + a_2 \hat{\delta} \mathbf{v}[k-1]$ , and applying the estimated disturbance  $\hat{\mathbf{w}}$  to compensate for  $\mathbf{w}$ , the control law achieving the control objective is expressed as superposition of the three components:

$$\mathbf{u}[k] = \mathbf{B}^{-1} \{ \mathbf{v}_{ff}[k] + \delta \mathbf{v}_{fb}[k] \} - \hat{\mathbf{w}}[k]. \quad (7)$$

Substituting (7) into (6), the tracking error dynamic is

$$\begin{aligned} \delta \mathbf{v}[k+1] &= \lambda_c \delta \mathbf{v}[k] - \mathbf{B} \mathbf{e}_w[k] \\ &\quad + (a_1 - \lambda_c) \mathbf{e}_{\delta \mathbf{v}}[k] + a_2 \mathbf{e}_{\delta \mathbf{v}}[k-1], \end{aligned} \quad (8)$$

where  $\mathbf{e}_w = \mathbf{w} - \hat{\mathbf{w}}$  and  $\mathbf{e}_{\delta \mathbf{v}} = \delta \mathbf{v} - \hat{\delta} \mathbf{v}$ . It is evident that the tracking performance improves as estimation errors are reduced. It is worth noting that the tracking error and the disturbance need to be successfully estimated to realize the proposed control law. An augmented state estimator [26], characterized by  $\lambda_e$ , is designed to achieve this objective. Let  $\mathbf{w}[k+1] = \mathbf{w}[k] + \delta \mathbf{w}[k]$  and denote  $\mathbf{s}_1[k] = \delta \mathbf{v}[k]$  and  $\mathbf{s}_2[k] = \delta \mathbf{v}[k-1]$ , the augmented state estimator is

$$\begin{cases} \hat{\mathbf{s}}_1[k+1] = \lambda_c \hat{\mathbf{s}}_1[k] + \mathbf{L}_1 \{ \delta \mathbf{v}[k] - \hat{\mathbf{s}}_1[k] \} \\ \hat{\mathbf{s}}_2[k+1] = \hat{\mathbf{s}}_1[k] + \mathbf{L}_2 \{ \delta \mathbf{v}[k] - \hat{\mathbf{s}}_1[k] \} \\ \hat{\mathbf{w}}[k+1] = \hat{\mathbf{w}}[k] + \delta \hat{\mathbf{w}}[k] + \mathbf{L}_3 \{ \delta \mathbf{v}[k] - \hat{\mathbf{s}}_1[k] \} \\ \delta \hat{\mathbf{w}}[k+1] = \delta \hat{\mathbf{w}}[k] + \mathbf{L}_4 \{ \delta \mathbf{v}[k] - \hat{\mathbf{s}}_1[k] \}, \end{cases} \quad (9)$$

where  $\mathbf{L}_i$  are the four  $6 \times 6$  feedback matrices of the estimator. Based on (8), i.e., the tracking error dynamic, the estimation error dynamics are

$$\begin{bmatrix} \mathbf{e}_{s_1}[k+1] \\ \mathbf{e}_{s_2}[k+1] \\ \mathbf{e}_w[k+1] \\ \mathbf{e}_{\delta w}[k+1] \end{bmatrix} = \begin{bmatrix} a_1 \mathbf{I} - \mathbf{L}_1 & a_2 \mathbf{I} - \mathbf{B} & 0 \\ \mathbf{I} - \mathbf{L}_2 & 0 & 0 & 0 \\ -\mathbf{L}_3 & 0 & \mathbf{I} & \mathbf{I} \\ -\mathbf{L}_4 & 0 & 0 & \mathbf{I} \end{bmatrix} \begin{bmatrix} \mathbf{e}_{s_1}[k] \\ \mathbf{e}_{s_2}[k] \\ \mathbf{e}_w[k] \\ \mathbf{e}_{\delta w}[k] \end{bmatrix}. \quad (10)$$

Assigning all eigenvalues to  $\lambda_e$ , the four feedback matrices of the estimator are

$$\begin{cases} \mathbf{L}_1 = (2 + a_1 - 4\lambda_e) \mathbf{I} \\ \mathbf{L}_2 = [1 + \lambda_e^4/a_2] \mathbf{I} \\ \mathbf{L}_3 = -(1 - \lambda_e)^3 (3 + \lambda_e) \mathbf{B}^{-1} \\ \mathbf{L}_4 = -(1 - \lambda_e)^4 \mathbf{B}^{-1} \end{cases}. \quad (11)$$

The control law, i.e., (7), and the augmented estimator, i.e., (9), are used to achieve two objectives, i.e., minimizing the uncertainty attributed to remanence and hysteresis, and increasing the bandwidth of magnetic flux generation. They are implemented using a high-speed FPGA system (Altera: Arria V GT) for real-time computation at 100 kHz. The frequency response of the six-input-six-output closed-loop magnetic flux control system (see Fig. 2) was experimentally evaluated. The value of  $\lambda_c$  associated with the control law is 0.9391 (1000 Hz) and that of

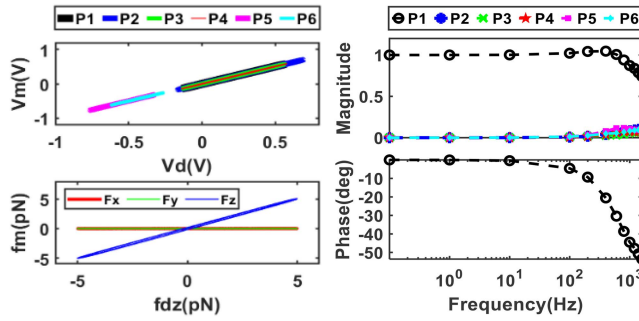


Fig. 4. Experimental results of closed-loop flux generation experiment.

$\lambda_e$  for the estimator is 0.7304 (5000 Hz). The voltage readings of all six Hall sensors were recorded.

The experimental results of closed-loop flux generation are presented in Fig. 4. The upper left panel presents the voltage readings of the six Hall sensors vs. the  $v_d$  associated with the 0.1Hz desired force along the z-direction. It clearly shows that the closed-loop flux control eliminates bias and hysteresis. The lower left panel presents the resulting magnetic force calculated using (3). It can be seen that the z-component of the generated magnetic force accords fully with the desired force and the other two components are zero. The results verify that the optimal flux allocation is accurate, and able to solve the four issues in multipole magnetic force generation: redundancy; coupling; nonlinearity; and position-dependency.

The right panel presents the frequency response curves of the six pole tips when the desired voltage for P1 is 2V and those for the other five poles are zeros. Similar results were obtained when different individual pole was selected in the experiment. It shows that while the hexapole actuation system has multipole coupling, uncertainties related to remanence and hysteresis, and limited bandwidth, with six-input-six-output flux control, the magnetic flux at each individual pole tip can be precisely controlled at frequencies up to 1000 Hz.

It is worth noting that the six-input-six-output magnetic flux control system is a sampled-data system with zero-order-hold and sampling. The exact discrete model of the sampled-data system has a zero close to  $-1$  in the  $z$ -plane [26]. However, the six-input-six-output model (6) used in the control law design is a discrete approximation that is accurate within a limited bandwidth. Therefore, the achieved closed-loop bandwidth for the magnetic flux control is limited to 1000 Hz.

#### D. Three-Input-Three-Output Force Generation System

Fig. 5 shows the real-time computation of optimal flux/voltage allocation of, and the magnetic flux control of, the three-input-three-output magnetic force generation system. In experiments, the desired force and the probe's position in the measurement coordinate system,  ${}^M\mathbf{f}_d$  and  ${}^M\mathbf{p}$ , are specified first, converted to the actuator coordinate system,  ${}^A\mathbf{f}_d$  and  ${}^A\mathbf{p}$ , then  $\mathbf{v}_{opt}$  obtained via optimal voltage allocation to serve as the input of the magnetic flux control system, i.e.,  $\mathbf{v}_d$ . The real-time computation for coordinate transformation and optimal voltage allocation operates

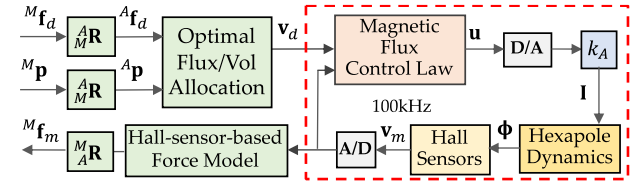


Fig. 5. Block diagram of the three-input-three-output force generation system.

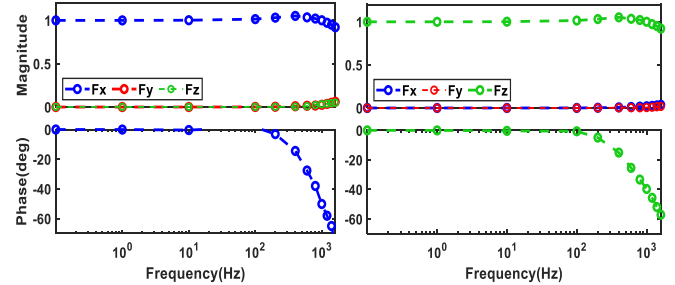


Fig. 6. Frequency response of the three input-3 output force generation system.

at 1.6 kHz, whereas the magnetic flux control is at 100 kHz. The output of the magnetic flux control  $\mathbf{v}_m$  is then used to calculate the 3-D magnetic force  ${}^M\mathbf{f}_m$ .

The frequency response of the three-input-three-output magnetic force generation system (see Fig. 5) was experimentally evaluated. In each experiment, the frequency of the desired force was increased from 0.1 Hz to 1.6 kHz while amplitude and desired force direction were held constant. The voltage readings of all six Hall sensors were recorded and used to calculate the resulting magnetic force to form frequency response curves. The left panel of Fig. 6 presents the frequency response curves associated with the 3-D output force when the desired force is 5 pN along the x-axis. The right panel presents the results when selecting the z-axis in the experiment. These results verify that together with optimal flux allocation, Hall-sensor-based magnetic flux control enables the six-input hexapole system to behave like a decoupled three-axis force producer with high bandwidth.

### III. UNTETHERED MANIPULATION OF MAGNETIC MICROPROBE

Fig. 7 shows the experimental setup for untethered manipulation of the magnetic probe in aqueous solutions, where the hexapole actuation system is integrated with an inverted microscope (Olympus IX 81). The z-axis of the measurement coordinate system is aligned with the optical axis of the microscope, intersecting the x-axis and the y-axis at the center of the workspace, and the objective focal plane is flush with the xy plane. The microscope is equipped with a vision-based 3-D particle tracking system to enable 3-D visual servo control.

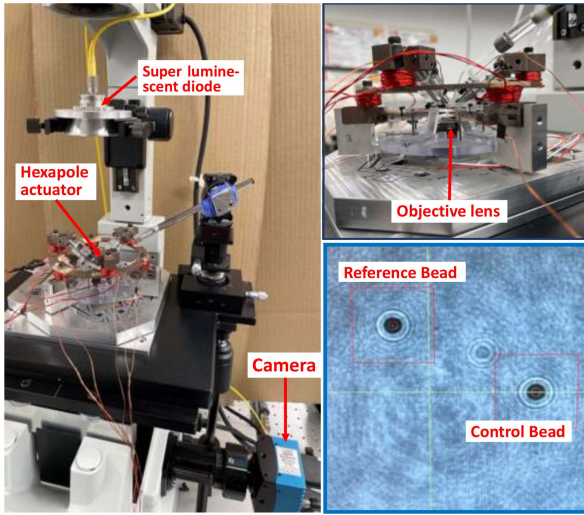


Fig. 7. Experimental setup for untethered manipulation of the magnetic probe in aqueous solutions.

#### A. Vision-Based 3-D Probe Tracking

The particle tracking system is an improved version of the first two implementations [27], [28] of the tracking algorithm based on microscope off-focus images, i.e., the image of a particle is correlated to its z-position, and this dependence is established by calibration prior to running the experiment. In the first implementation [27], the radial projection of the acquired image is compared to the calibrated model to determine the axial position ( $z$ ) using a least-squares matching algorithm, while estimating the transverse position of the particle ( $x, y$ ) from the acquired image using a widely accepted centroid method [29]. The total time delay attributed to image acquisition, data transmission, and real-time computation is the two steps of the sampling cycle. The system was used in [22] to achieve visual servo control of magnetic microbeads in water.

In the second implementation [28], the system uses a high-speed CMOS camera (Mikrotron: MC3010) for image acquisition and a FPGA board for real-time computation. The camera acquires images of  $128 \times 128$  pixels at a frame rate of up to 10000 frames per second (fps) under the white light illumination from a standard 100 W halogen lamp. Two important objectives had been achieved: real-time estimation of the 3-D position matches the maximum frame rate of the camera and the timing of the output data stream of the system is precisely controlled. While both implementations achieve nanoresolution, measurement is biased due to the asymmetry of the image and the use of radial projection.

The newest implementation of the system has two major improvements over the second implementation. First, a superluminescent diode illumination system is used to further enhance the image sensitivity and improve the measurement resolution in both transverse directions and the axial direction. Second, instead of using the centroid method and the radial projection, the transverse position of the probe is determined using the continuous image registration method [30], and an optimal matching technique is used to compare the off-focus

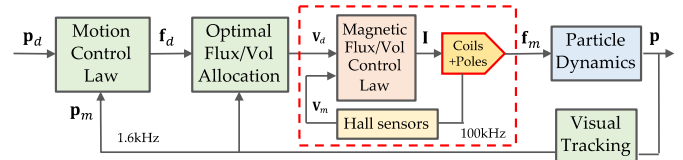


Fig. 8. Block diagram of a visual servo control for untethered manipulation of the magnetic probe in aqueous solutions.

2-D image to the calibrated object-specific model to estimate the axial position [31]. With the second improvement, the system achieves zero-bias measurements.

The bottom right panel of Fig. 7 shows a snapshot of measuring the immobilized reference bead and the moving probe simultaneously. This dual-bead tracking allows for drift compensation and low frequency vibration cancellation. Since it requires a larger region of interest, i.e.,  $512 \times 512$  pixels, the sampling rate of visual servo control is 1.6 kHz. It has been experimentally verified that when using the  $60\times$  magnification lens, the measurement resolution for a spherical probe with a radius of  $2.25 \mu\text{m}$  is about 0.7 nm (rms) in both the  $x$ - and  $y$ -directions, and 2.3 nm (rms) in the  $z$ -direction.

#### B. Visual Servo Control

The dynamics of microscopic probes moving in aqueous solutions are governed by the Langevin equation at low Reynolds numbers [32], driven by controllable electromagnetic forces and influenced by random thermal forces. The equation for 3-D motion is given as follows:

$$\gamma \dot{\mathbf{p}}(t) = \mathbf{f}_m(\mathbf{p}(t), \mathbf{I}(t)) + \mathbf{f}_T(t), \quad (12)$$

where  $\gamma$  is the drag coefficient, characterized by Stokes' law for spherical probes, i.e.,  $\gamma = 6\pi\eta R$ , where  $\eta$  is the dynamic viscosity of the solution,  $R$  probe radius,  $\mathbf{p}$  probe position,  $\mathbf{I}$  the vector of the six input currents applied to the hexapole actuator,  $\mathbf{f}_T$  random thermal force, and  $\mathbf{f}_m$  magnetic force, respectively.

The hexapole actuator uses the six input currents to produce magnetic fluxes  $\phi(\mathbf{I}(t))$  at the six pole tips to control the magnetic field in the 3-D workspace and to generate 3-D magnetic force,  $\mathbf{f}_m(\mathbf{p}(t), \mathbf{I}(t)) = g_\phi \phi^T(\mathbf{I}(t)) \mathbf{L}(\hat{\mathbf{p}}) \phi(\mathbf{I}(t))$ , exerted on the magnetic probe. There are, however, challenges when using the hexapole actuator to undertake untethered manipulation of the magnetic probe in aqueous solutions. First, the hexapole actuator is an over-actuated system, and the generation of magnetic force is position dependent. Second, the flux generation process  $\phi(\mathbf{I}(t))$  suffers from uncertainty attributed to remanence and hysteresis and involve multipole coupling and dynamics. Third, one can use the Jacobian matrix,  $\partial \mathbf{f}_m / \partial \mathbf{p}$ , to verify that the dynamic system in (12) is an unstable system.

A visual servo control system is designed and implemented to address these challenges. Its block diagram is shown in Fig. 8. The 3-D tracking system operates at the sampling rate of 1.6 kHz, providing the 3-D position of the probe with nanometer precision in real time. The control system is composed of three core components. The optimal voltage allocation solves four issues:

redundancy; coupling; nonlinearity; and position-dependency. The magnetic flux control significantly suppresses the uncertainty due to remanence and hysteresis and greatly increases the bandwidth of the flux generation. The motion control law determines the desired force for stabilization and propulsion. It was shown in Section II that with the optimal flux allocation and the closed-loop flux control, the six-input hexapole actuator can be treated as a linear decoupled three-axis force producer with a bandwidth of 1000 Hz.

When operating the visual servo control loop below its bandwidth of 1000 Hz, the resulting magnetic force is close to the desired force determined by the laws of motion control, i.e.,  $\mathbf{f}_m(t) \approx \mathbf{f}_d(t)$ . Since the 3-D motion of the probe being controlled is decoupled, for simplicity, the equations for 1-D motion are given in the following analysis:

$$\gamma \dot{x}(t) = f_d(t) + f_T(t). \quad (13)$$

Since the control law is realized in the form of digital calculation, integrating  $\dot{x}$  over one sampling period, the discrete-time equation of motion of the sampled-data system is

$$x[k+1] = x[k] + \frac{\Delta t}{\gamma} (f_d[k] + f_T[k]), \quad (14)$$

where  $\Delta t$  is the sampling period and  $f_d$  is the desired force to be determined from the control law and to be realized by applying the optimal flux allocation and the closed-loop magnetic flux control. The thermal force experienced by the probe  $f_T$  is quantified by variance  $\sigma_{f_T}^2 = 4k_B T \gamma / \Delta t$  [33], which is proportional to  $\gamma$  and inversely proportional to  $\Delta t$ , where  $k_B$  is the Boltzmann's constant and  $T$  is the absolute temperature of the aqueous solution.

Let the control objective be  $\delta x[k+1] = \lambda_c \cdot \delta x[k]$ , where  $\delta x[k] = x_d[k] - x[k]$ , and  $x_d[k]$  is the desired motion trajectory, comparing (14) with the desired motion, the force required to meet the control objective can be obtained

$$f_d[k] = \frac{\gamma}{\Delta t} \{x_d[k+1] - \lambda_c x_d[k] - (1 - \lambda_c)x[k]\} - f_T[k]. \quad (15)$$

If the measurement has a  $d$ -step delay, i.e.,  $x_m[k] = x[k-d]$ ,  $x[k]$  in (15) can be related to  $x_m[k]$  according to (14)

$$x[k] = x_m[k] + \frac{\Delta t}{\gamma} \left( \sum_{i=1}^d (f_d[k-i] + f_T[k-i]) \right). \quad (16)$$

A discrete-time control law, subject to the  $d$ -step measurement delay, is

$$\begin{aligned} f_d[k] &= \frac{\gamma}{\Delta t} \{x_d[k+1] - \lambda_c x_d[k] - (1 - \lambda_c)x_d[k-d] \\ &\quad + (1 - \lambda_c)\delta x_m[k]\} - (1 - \lambda_c) \sum_{i=1}^d f_d[k-i], \end{aligned} \quad (17)$$

where  $\delta x_m[k] = \delta x[k-d] + n_x[k]$ , and  $n_x[k]$  is the measurement noise. Substituting (17) into (14) and comparing the resulting motion with the desired motion trajectory, the dynamics

of the tracking error can be derived

$$\delta x[k+1] = \lambda_c \cdot \delta x[k] - \varepsilon[k], \quad (18)$$

where  $\varepsilon[k]$  is a zero-mean random variable related to thermal force, measurement noise, and  $\lambda_c$ , i.e.,

$$\begin{aligned} \varepsilon[k] &= (\Delta t / \gamma) \left\{ f_T[k] + (1 - \lambda_c) \sum_{i=1}^d f_T[k-i] \right\} \\ &\quad + (1 - \lambda_c) n_x[k]. \end{aligned} \quad (19)$$

Therefore, the tracking error is a zero-mean random error, dictated by both thermal forces and measurement noise.

### C. Variance Control of the Tracking Error

According to (18) and (19), the tracking error is attributed to two sources, i.e., thermal forces and measurement noise. By using z-transform, (18) and (19) can be rewritten as

$$\delta x(z^{-1}) = -H_T(z^{-1}) \delta x_T(z^{-1}) - H_n(z^{-1}) n_x(z^{-1}), \quad (20)$$

where  $\delta x_T$  denotes thermal motion, i.e.,  $\delta x_T = (\Delta t / \gamma) f_T$ , and  $H_T$  and  $H_n$  are two transfer functions. The variance of the tracking error can then be derived [34]. Since our motion tracking system has a two-step measurement delay,  $d = 2$ , the two transfer functions are given as

$$\begin{cases} H_T(z^{-1}) = z^{-1} \frac{1+(1-\lambda_c)z^{-1}+(1-\lambda_c)z^{-2}}{1-\lambda_c z^{-1}} \\ H_n(z^{-1}) = z^{-1} \frac{1-\lambda_c}{1-\lambda_c z^{-1}} \end{cases}. \quad (21)$$

They are used to derive the variance of the tracking error

$$\sigma_{\delta x}^2 = \left( 2 + \frac{1}{1 - \lambda_c^2} \right) \sigma_{\delta x_T}^2 + \left( \frac{1 - \lambda_c}{1 + \lambda_c} \right) \sigma_{n_x}^2, \quad (22)$$

where  $\sigma_{\delta x_T}^2 = (\Delta t / \gamma)^2 \sigma_{f_T}^2 = 4k_B T \Delta t / \gamma$  is the variance of thermal motion. The variance is a linear superposition of the thermal motion variance ( $\sigma_{\delta x_T}^2$ ) and the measurement noise variance ( $\sigma_{n_x}^2$ ) and is controlled by selecting the design value  $\lambda_c$ . Denoting the ratio between  $\sigma_{n_x}^2$  and  $\sigma_{\delta x_T}^2$  as  $r_{\sigma^2}$ , the design achieving minimum-variance control can be derived as follows:

$$\lambda_c = \lambda_{\delta x_{\min}} = 1 - \frac{1}{2r_{\sigma^2}} \left[ \sqrt{1 + 4r_{\sigma^2}} - 1 \right] \quad (23)$$

and

$$\sigma_{\delta x_{\min}}^2 = \frac{1}{2} \sigma_{\delta x_T}^2 \left( \sqrt{1 + 4r_{\sigma^2}} + 5 \right). \quad (24)$$

Experiments are used to verify the tracking performance described in (18), i.e., the mean of the tracking errors is zero, and the variance of random motion depends on  $\lambda_c$  predicted in (22). The commanded motion is a plane motion in the  $xy$  plane of the measurement coordinate system, wherein both the  $x$ -axis and  $y$ -axis motions are sine waves with an amplitude of 3.74  $\mu\text{m}$  and a frequency of 5 Hz. Since the plane motion is 15 micrometers above the bottom coverslip,  $r_{\sigma^2}$  for both the  $x$ -axis and  $y$ -axis motions is 0.489. The resulting motion of each experiment was recorded, the mean of the tracking error was verified to be zero, and the variance and standard deviation of the tracking error were calculated. Fig. 9 presents

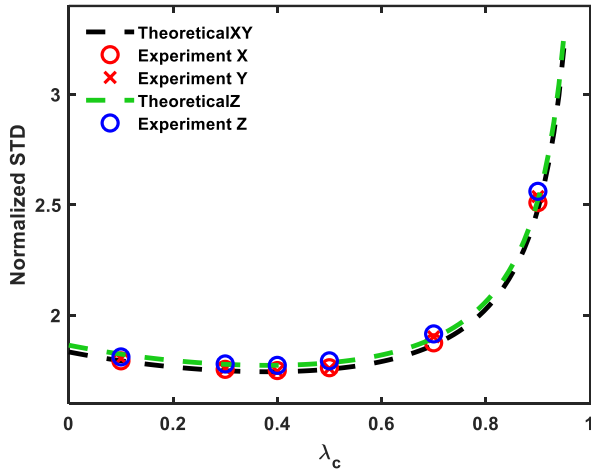


Fig. 9. Normalized standard deviation of the tracking error, compared with the theoretical predictions.

the normalized standard deviation of the tracking errors for six experiments with different  $\lambda_c$ , i.e.,  $\lambda_c = 0.1, 0.3, 0.4, 0.5, 0.7$ , and  $0.9$ . They are normalized by the standard deviation of thermal motion and compared to theoretical predictions. It is worth noting that the measurement noise of the  $z$ -axis is greater than the measurement noise of the  $x$ - and  $y$ -axes. Therefore, the tracking error has a slightly larger standard deviation on the  $z$ -axis.

#### D. Spatially Correlated Drag Coefficient

As the probe moves close to a wall, the drag coefficient varies with its distance from the surface. Displacement along two principle directions, perpendicular and parallel to the wall, and a dimensionless variable  $h/R$  characterize the position-dependent drag coefficient, i.e.,  $\gamma_{\perp} = 6\pi\eta R \cdot C_{\perp}(h/R)$  and  $\gamma_{\parallel} = 6\pi\eta R \cdot C_{\parallel}(h/R)$ , where  $\eta$  is the dynamic viscosity,  $R$  is the radius of the probe, and  $h$  is the distance from the center of the probe to the wall.  $C_{\perp}(h/R)$  and  $C_{\parallel}(h/R)$  are two known dimensionless functions [35], [36]. The local drag coefficient  $\gamma(\mathbf{p})$  can be accurately determined using the variance of the probe's Brownian motion [37]. It can be done either using real-time estimation or by calibration prior to running experiments.

For simplicity, the latter approach is used. A spherical probe with a radius of  $2.25 \mu\text{m}$  was used to calibrate the position-dependent drag coefficient. In the experiment, the wall surface was the top surface of the culture dish, which was about 15 micrometers below the  $xy$  plane of the measurement coordinate system. The probe was sequentially moved to nine different heights, where Brownian motion was recorded. The variance was calculated and then used to fit both nominal gamma and wall height. The obtained nominal gamma,  $\gamma_N = 0.0424 (\text{pN} \cdot \text{sec}/\mu\text{m})$  is very close to the value from Stokes' law,  $6\pi\eta R = 0.042412 (\text{pN} \cdot \text{sec}/\mu\text{m})$ , and  $w = -14.0394 (\mu\text{m})$ . In addition, the normalized position-dependent drag coefficients accord well with known  $C_{\perp}(h/R)$  and  $C_{\parallel}(h/R)$ . The parameter  $\gamma$  in the discrete time control law described in

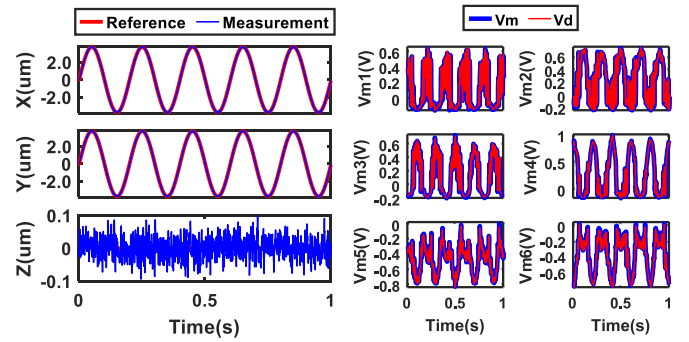


Fig. 10. 2-D sine wave tracking: the left panel presents the resulting motion, and the right panel presents the voltage readings of the six Hall sensors compared with the desired voltages from the optimal voltage allocation.

(17) is now position-dependent (time-varying), and is written as  $\gamma_{x/y}(h/R) = \gamma_N \cdot C_{\parallel}(h/R)$  and  $\gamma_z(h/R) = \gamma_N \cdot C_{\perp}(h/R)$ , where  $h[k] = z[k] - w$ .

#### IV. EXPERIMENTAL VERIFICATION OF ULTRAPRECISE HIGH-SPEED UNTETHERED MANIPULATION

In this section, experimental results are used to demonstrate the significance and effectiveness of the three core functions of the control system, namely the closed-loop magnetic flux control, the optimal magnetic flux allocation, and time-varying discrete-time motion control law. In all experiments,  $\lambda_c = 0.4$  is the value used in the discrete-time motion control law.

##### A. Zero-Mean Tracking Error

In the first experiment, the magnetic probe was propelled to move in the  $xy$  plane, where both the  $x$ -axis and  $y$ -axis motions being sine waves with an amplitude of  $3.74 \mu\text{m}$  and a frequency of 5 Hz. In the second experiment, the commanded motion changed from a sine wave to a triangle wave. Fig. 10 presents the experimental results of the 2-D sine wave tracking when all three core functions being used to render motion control. The left panel presents the resulting motion. The mean and standard deviation of the tracking errors of all three axes were calculated and compared with their respective theoretical predictions. As expected, the mean of each axis is close to zero ( $< 0.8 \text{ nm}$ ). The standard deviation of each axis is  $\hat{\sigma}_{\delta x} = 32.29 \text{ nm}$ ,  $\hat{\sigma}_{\delta y} = 32.10 \text{ nm}$ , and  $\hat{\sigma}_{\delta z} = 30.88 \text{ nm}$ , close to their predicted values,  $\sigma_{\delta x/\delta y} = 31.97 \text{ nm}$  and  $\sigma_{\delta z} = 30.69 \text{ nm}$ . It is worth noting that these random errors are attributed to random thermal forces and random measurement noise. The right panel presents the voltage readings of the six Hall sensors compared with the desired voltages from the optimal voltage allocation. It shows that the closed-loop flux control be able to adjust the six actuation currents to generate the fluxes to follow their desired values at the six pole tips.

Fig. 11 presents the experimental results of the 2-D triangle wave tracking. The left panel presents the resulting motion. The mean and standard deviation of the tracking errors are calculated.

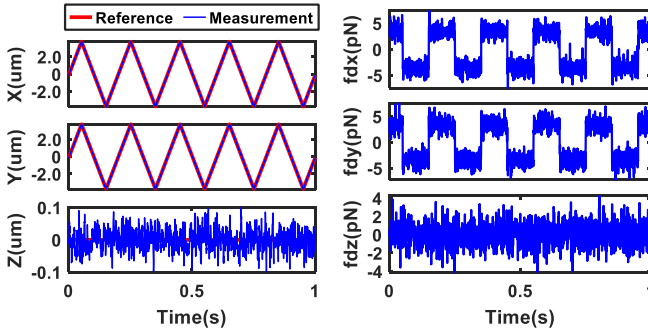


Fig. 11. 2-D triangle wave tracking: the left panel presents the resulting motion, and the right panel presents the three components of the desired force from the discrete-time control law.

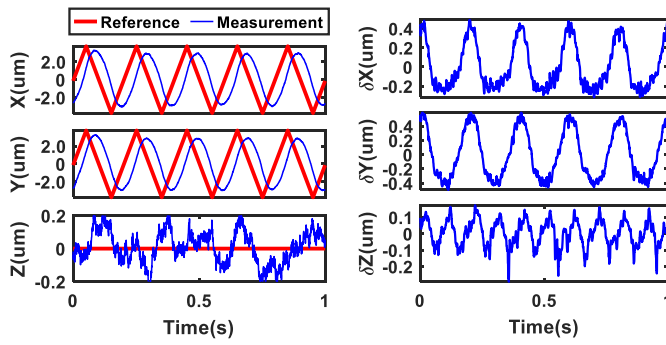


Fig. 12. 2-D motion tracking: the left panel presents the resulting triangular motion when replacing the motion control law with a PI controller, and the right panel shows the motion errors in the sine wave tracking when the closed-loop flux control was not used.

The mean is again close to zero. The standard deviation for each axis is  $\hat{\sigma}_{\delta x} = 32.17 \text{ nm}$ ,  $\hat{\sigma}_{\delta y} = 32.12 \text{ nm}$ , and  $\hat{\sigma}_{\delta z} = 30.73 \text{ nm}$ , close to their predicted values. The right panel presents the desired force determined by the discrete-time control law. It shows that the desired force has two main components, the square wave generated for the feedforward control and the high-frequency feedback control effort for stabilization. These results verify that the proposed motion control law achieves superior motion tracking independent of the reference motion trajectory, provided that the actuator can provide the required control force.

Two additional experiments are used to demonstrate the significance of the core functions of the control system. Fig. 12 presents the experimental results of 2-D motion tracking. The left panel presents the resulting triangular motion when replacing the motion control law with a PI controller. The results show that there is obvious phase lag in the 2-D motion, and there is a deterministic error in the  $z$ -axis motion. The right panel presents the motion errors in the sine wave tracking when the closed-loop flux control was not used. The results show that while the optimal flux allocation attempted to distribute the six actuation currents according to the desired force, the errors in magnetic flux generation were too large to be overcome by the motion control law. Specifically, deterministic errors are evident on all three axes.

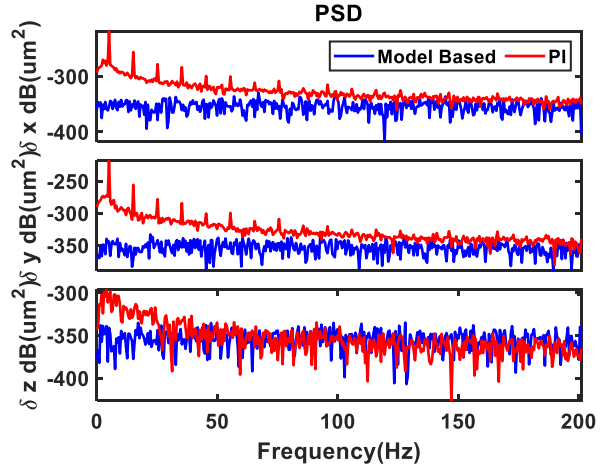


Fig. 13. Measured power spectral density of the tracking error: red curve is associated with the PI motion controller and blue curve is associated with the proposed motion control law.

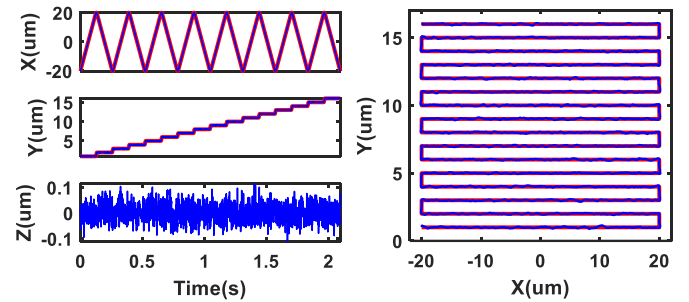


Fig. 14. 2-D raster scan motion: the left panel shows the resulting motion, and the right panel shows the resulting scan pattern.

Fig. 13 compares the measured PSD of the tracking error associated with the two triangle-wave-tracking experiments. It can be seen the tracking error associated with the proposed motion control law is very close to the random error, whereas the PSD associated with the PI motion controller exhibits peaks at the frequency of the triangle wave (5 Hz) and its harmonics.

### B. Two-Dimensional High-Speed Scanning Motion

To demonstrate the feasibility of rendering high-speed SPM using the integrated control system, it was applied to perform scanning motion control. Fig. 14 presents the experimental results of 2-D raster scanning motion of the magnetic probe in aqueous solutions, where the probe was controlled to scan over a rectangular area of  $40 \mu\text{m} \times 16 \mu\text{m}$  in the  $xy$  plane within two seconds. The left panel shows the resulting motion of three separate axes, and the right panel shows the resulting scan pattern. The mean and standard deviation of the motion error are calculated to verify the expected performance of raster scanning motion, i.e., the mean of the motion error for each axis is close to zero and the standard deviation for each axis close to the predicted value. It is worth noting that the experiment aimed to demonstrate the ability of high-speed motion control required in raster scanning. It was not an actual scanning, which requires

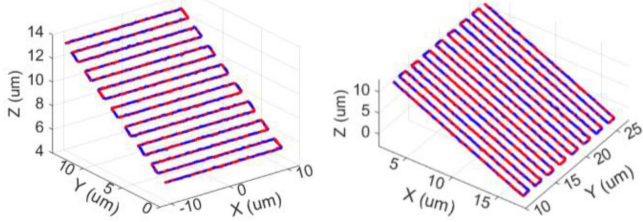


Fig. 15. 2-D raster scan motion in inclined planes.

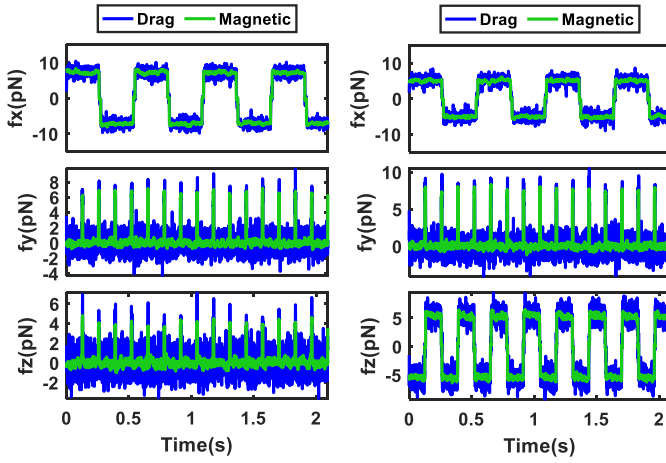


Fig. 16. Comparison of the generated magnetic force with the drag force experienced by the magnetic probe in two oblique plane scan experiments.

force control on the  $z$ -axis. Nonetheless, the achieved motion range and the scan frame rate suggest that the integrated system can be used to render live cell scanning.

Fig. 15 presents two 2-D raster scan patterns on two different inclined planes for two separate experiments. They show that the motion control system can be used to control the magnetic probe to undertake raster scanning with different scan patterns and on any oblique planes. Fig. 16 presents the generated magnetic force compared with the drag force experienced by the magnetic probe in the two oblique plane scan experiments. The Hall-sensor-based hexapole magnetic force model, (3), is used to calculate the resulting 3-D magnetic force  ${}^M\mathbf{f}_m({}^M\mathbf{p}, \mathbf{v}_m)$ , and the drag force is  $\gamma({}^M\mathbf{p}){}^M\dot{\mathbf{p}}$ . It is worth noting that the magnetic force is the drag force minus the thermal force, i.e.,  $\mathbf{f}_m = \gamma\dot{\mathbf{p}} - \mathbf{f}_T$ . The results verify the accuracy of the Hall-sensor-based hexapole force model, of the optimal magnetic flux allocation, and of the closed-loop magnetic flux control.

### C. Three-Dimensional Rapid Steering

Fig. 17 presents the experimental results of 3-D rapid steering of the magnetic probe in aqueous solutions, where the probe was steered to follow a specified conical helix in the workspace. The probe started from the initial position of  $(0 \mu\text{m}, 0 \mu\text{m}, 0 \mu\text{m})$ , was controlled to rotate along the upward pitch for five cycles, each cycle taking 0.35 s, reached the highest point  $(30 \mu\text{m}, 0 \mu\text{m}, 15 \mu\text{m})$ , and then was steered back to the

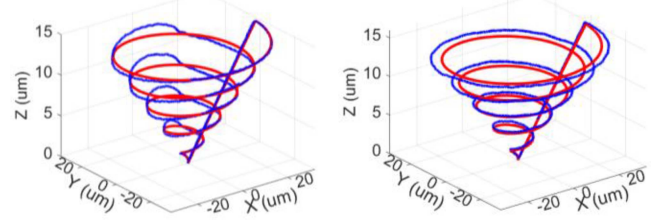


Fig. 17. 3-D rapid steering: the left panel shows the resulting motion when the closed-loop flux control was not used, and the right panel shows the resulting motion when replacing the motion control law with a PI controller.

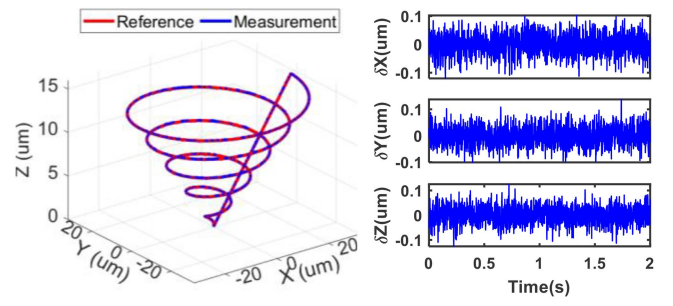


Fig. 18. 3-D rapid steering: the left panel shows the resulting motion, and the right panel shows the tracking error.

initial position in 0.25 s. The left panel presents the resulting motion when the closed-loop flux control was not used. The results show that the error in magnetic flux generation was large, which greatly degraded the steering performance. Nonetheless, the motion control law was able to stabilize the 3-D motion. The right panel presents the resulting motion when replacing the motion control law with a PI controller. The results show that the 3-D motion has a significant phase lag.

Fig. 18 shows the experimental results of 3-D rapid steering when all three core functions were used to render high-speed visual servo control. The left panel presents the resulting 3-D motion, and the right panel presents the tracking errors of the three axes. As expected, the results show superior performance for rapid 3-D steering with no deterministic errors in any of the three axes. The standard deviation of the random error for each axis is close to the theoretical prediction.

## V. CONCLUSION AND DISCUSSION

An integrated control system has been designed and developed to render ultraprecise and high-speed untethered manipulation of a single magnetic scanning probe in aqueous solutions under a microscope. The control system uses a hexapole electromagnetic actuator to control the magnetic field in the 3-D workspace and the 3-D magnetic force exerted on the magnetic scanning probe. It uses a vision-based 3-D particle tracking system to enable visual servo control. Three core functions have been designed and implemented to achieve superior manipulation of the magnetic microprobe. The six-input-six-output closed-loop magnetic flux control suppresses the effect of hysteresis and greatly increases the bandwidth of magnetic

flux generation. The optimal voltage allocation, minimizing the two-norm of the magnetic flux vector, solves four issues in multipole magnetic force generation: redundancy; coupling; nonlinearity; and position-dependency. The position-dependent discrete-time motion control law determines the required force for stabilization and tracking.

The experimental results of magnetic flux control show that the closed-loop system can adjust the six actuation currents to generate magnetic fluxes at the six pole tips to follow their desired values at frequencies up to 1000 Hz. The experimental results of motion control verify that together with the magnetic flux control, independent of the desired motion trajectory, the position-dependent discrete-time motion control law achieves superior tracking performance, wherein the motion error is zero-mean random error, and its variance can be analytically predicted and determined by random thermal forces and random measurement noise. The experimental results of raster scanning demonstrate that the integrated system can be used to control the magnetic microprobe to undertake raster scanning in the 3-D workspace.

There are several aspects that can be worked on to improve the functionality of the control system. First, it is necessary to design the control law using the exact discrete model of the sampled-data system to achieve greater bandwidth for the six-input-six-output magnetic flux control system. The exact discrete model of the sampled-data system with zero-order-hold and sampling has a zero close to  $-1$  in the  $z$ -plane [26]. When using the direct design method (7) to design the control law, it causes instability or ringing. Therefore, control methods specific to non-minimum phase systems [38] will be used to achieve precise magnetic flux control of high bandwidth. Second, when using the integrated system to control the motion of a probe with a radius of  $2.25 \mu\text{m}$  in aqueous solution at room temperature, the standard deviation of the thermal motion is about 32 nm. The only way to reduce thermal motion is to increase the sampling rate of the visual servo control system. Third, when applying the control system in an unstructured test environment, the ability to estimate the position-dependent drag coefficients in real time is necessary. Fourth, the control of probe-sample interaction is one of the valuable and challenging applications of the system. It lays the foundation for automatic scanning, controlled probing, and untethered manipulation of biological samples.

#### ACKNOWLEDGMENT

The authors would like to thank the anonymous reviewers for their careful reading of our manuscript and their many insightful comments and suggestions.

#### REFERENCES

- [1] S. Suresh, "Biomechanics and biophysics of cancer cells," *Acta Biomater.*, vol. 3, no. 4, pp. 413–438, Jul. 2007.
- [2] D. J. Müller et al., "Atomic force microscopy of native purple membrane," *Biochimica Biophysica Acta, Bioenergetics*, vol. 1460, pp. 27–38, 2000.
- [3] C. Huang, C. F. Wang, D. S. Mehta, and A. Chiou, "Optical tweezers as sub-pico-newton force transducers," *Opt. Commun.*, vol. 195, pp. 41–48, 2001.
- [4] W. Singer, S. Bernet, N. Hecker, and M. Ritsch-Martens, "Three-dimensional force calibration of optical tweezers," *J. Modern Opt.*, vol. 47, pp. 2921–2931, 2000.
- [5] A. L. Stout, "Detection and characterization of individual intermolecular bonds using optical tweezers," *Biophys. J.*, vol. 80, no. 6, pp. 2976–2986, 2001.
- [6] P. M. Hansen, V. K. Bhatia, N. Harrit, and L. Oddershede, "Expanding the optical trapping range of gold nanoparticles," *Nano Lett.*, vol. 5, no. 10, pp. 1937–1942, 2005.
- [7] Y. Seol, A. E. Carpenter, and T. T. Perkins, "Gold nanoparticles: Enhanced optical trapping sensitivity coupled with significant heating," *Opt. Lett.*, vol. 31, pp. 1678–1680, 2006.
- [8] E. Peterman, F. Gittes, and C. F. Schmidt, "Laser-induced heating in optical traps," *Biophys. J.*, vol. 84, pp. 1308–1316, 2003.
- [9] Y. Huang, J. Wan, M. C. Cheng, Z. Zhang, S. Jhiang, and C. H. Menq, "Three-axis rapid steering of optically propelled micro/nano particles," *Rev. Sci. Instrum.*, vol. 80, 2009, Art. no. 063107.
- [10] J. Wan, Y. Huang, S. Jhiang, and C. H. Menq, "Real-time in situ calibration of an optically trapped probing system," *Appl. Opt.*, vol. 48, pp. 4832–4841, 2009.
- [11] Z. Zhang and C. Menq, "Six-axis magnetic levitation and motion control," *IEEE Trans. Robot.*, vol. 23, no. 2, pp. 196–205, Apr. 2007.
- [12] S. K. Kuo, X. Shan, and C. H. Menq, "Large travel ultra precision X-Y-Theta motion control of a magnetic suspension stage," *IEEE/ASME Trans. Mechatronics*, vol. 8, no. 3, pp. 334–341, Sep. 2003.
- [13] T. Honda, K. I. Arai, and K. Ishiyama, "Micro swimming mechanisms propelled by external magnetic fields," *IEEE Trans. Magn.*, vol. 32, no. 5, pp. 5085–5087, Sep. 1996.
- [14] L. Zhang, J. J. Abbott, L. X. Dong, B. E. Kratochvil, D. Bell, and B. J. Nelson, "Artificial bacterial flagella: Fabrication and magnetic control," *Appl. Phys. Lett.*, vol. 94, 2009, Art. no. 064107.
- [15] Y. Jeong, G. R. Jayanth, S. M. Jhiang, and C. H. Menq, "Design and fabrication of an active Multi-axis probing system for High-speed atomic force microscopy," *IEEE Trans. Nanotechnol.*, vol. 9, no. 3, pp. 392–399, May 2010.
- [16] G. R. Jayanth and C. H. Menq, "Two-axis force sensing and control of a re-orientable scanning probe," *IEEE/ASME Trans. Mechatronics*, vol. 18, no. 2, pp. 687–696, Apr. 2013.
- [17] K. C. Neuman and A. Nagy, "Single-molecule force spectroscopy: Optical tweezers, magnetic tweezers and atomic force microscopy," *Nature Methods*, vol. 5, no. 6, pp. 491–505, Jun. 2008.
- [18] J. T. Finer, R. M. Simmons, and J. A. Spudich, "Single myosin molecule mechanics - Piconewton Forces and nanometer steps," *Nature*, vol. 368, no. 6467, pp. 113–119, Mar. 1994.
- [19] C.-H. Chiou, Y.-Y. Huang, M.-H. Chiang, H.-H. Lee, and G.-B. Lee, "New magnetic tweezers for investigation the mechanical properties of single DNA molecules," *Nanotechnology*, vol. 17, pp. 1217–1224, 2006.
- [20] N. Walter, C. Selhuber, H. Kessler, and J. P. Spatz, "Cellular unbinding forces of initial adhesion processes on nanopatterned surfaces probed with magnetic tweezers," *Nano Lett.*, vol. 6, no. 3, pp. 398–402, Mar. 2006.
- [21] D. Salas, V. Gocheva, and M. Nöllmann, "Constructing a magnetic tweezers to monitor RNA translocation at the single-molecule level," in *RNA Remodeling Proteins*, New York, NY, USA: Springer, 2015, pp. 257–273.
- [22] Z. Zhang, F. Long, and C. Menq, "Three-Dimensional visual servo control of a magnetically propelled microscopic bead," *IEEE Trans. Robot.*, vol. 29, no. 2, pp. 373–382, Apr. 2013.
- [23] F. Long, D. Matsuuwa, and C. Menq, "Actively controlled hexapole electromagnetic actuating system enabling 3-D force manipulation in aqueous solutions," *IEEE/ASME Trans. Mechatronics*, vol. 21, no. 3, pp. 1540–1551, Jun. 2016.
- [24] F. Long, P. Cheng, T. M. Meng, and C. -H. Menq, "Optimal current allocation rendering 3-D magnetic force production in hexapole electromagnetic actuation," *IEEE/ASME Trans. Mechatronics*, vol. 26, no. 5, pp. 2408–2417, Oct. 2021.
- [25] F. Long, T. -M. Meng, J. -J. Wang, and C. -H. Menq, "Hall-Sensor-Based magnetic force modeling and inverse modeling for hexapole electromagnetic actuation," *IEEE/ASME Trans. Mechatronics*, to be published, doi: [10.1109/TMECH.2021.3113273](https://doi.org/10.1109/TMECH.2021.3113273).
- [26] G. F. Franklin, J. D. Powell, and M. Workman, *Digital Control of Dynamic Systems*, 3rd ed. Menlo Park, CA, USA: Addison-Wesley, 1998.

- [27] Z. Zhang and C.-H. Menq, "Three-Dimensional particle tracking with subnanometer resolution using off-focus images," *Appl. Opt.*, vol. 47, no. 14, pp. 2361–2370, 2008.
- [28] P. Cheng, S. M. Jhiang, and C. H. Menq, "Real-time visual sensing system achieving high-speed 3D particle tracking with nanometer resolution," *Appl. Opt.*, vol. 52, no. 31, pp. 7530–7539, Nov. 2013.
- [29] J. Arines and J. Ares, "Minimum variance centroid thresholding," *Opt. Lett.*, vol. 27, pp. 497–499, 2002.
- [30] P. Cheng and C. Menq, "Real-time continuous image registration enabling ultra-precise two-dimensional motion tracking," *IEEE Trans. Image Process.*, vol. 22, no. 5, pp. 2081–2090, May 2013.
- [31] P. Cheng and C. Menq, "Visual tracking of six-axis motion rendering ultraprecise visual servoing of microscopic objects," *IEEE/ASME Trans. Mechatronics*, vol. 23, no. 4, pp. 1564–1572, Aug. 2018.
- [32] W. Coffey, Y. P. Kalmykov, and J. Waldron, *The Langevin Equation: With Applications to Stochastic Problems in Physics, Chemistry and Electrical Engineering*, 2nd ed., Singapore: World Sci. Publ., 2004.
- [33] A. Papoulis and S. U. Pillai, *Probability, Random Variables, and Stochastic Process*, 4th ed. Boston, MA, USA: McGraw-Hill, 2002.
- [34] J.-Q. Sun, *Stochastic Dynamics and Control*, New York, NY, USA: Elsevier, 2006.
- [35] E. Schäffer, S. F. Nørrelykke, and J. Howard, "Surface forces and drag coefficients of microspheres near a plane surface measured with optical tweezers," *Langmuir*, vol. 23, pp. 3654–3665, 2007.
- [36] K. C. Neuman and S. M. Block, "Optical trapping," *Rev. Sci. Instrum.*, vol. 75, pp. 2787–2809, 2004.
- [37] F. Gittes and C. F. Schmidt, "Thermal noise limitations on micromechanical experiments," *Eur. Biophys. J.*, vol. 27, pp. 75–81, 1998.
- [38] J. Xia and C. H. Menq, "Precision tracking control of non-minimum phase systems with zero phase error," *Int. J. Control.*, vol. 61, no. 4, pp. 791–807, 1995.



**Ta-Min Meng** received the B.S. degree in power mechanical engineering from the National Tsing Hua University, Hsinchu, Taiwan, in 2015. He is currently working toward the Ph.D. degree with the Department of Mechanical and Aerospace Engineering, The Ohio State University, Columbus, OH, USA.

His research interests include modeling, estimation, sensing, and control of precision electromechanical systems.



**Chia-Hsiang Menq** received the Ph.D. degree in mechanical engineering from Carnegie Mellon University, PA, USA, in 1985.

Since 1985, he has been with the Ohio State University, OH, USA. He has been the holder of the Ralph W. Kurtz Endowed Chair in Mechanical Engineering with The Ohio State University since 2006.

Dr. Menq is a fellow of the American Society of Mechanical Engineers, the American Association for the Advancement of Science, and the Society of Manufacturing Engineers.